International Journal of Rock Mechanics & Mining Sciences 46 (2009) 555–567

Contents lists available at ScienceDirect

International Journal of Rock Mechanics & Mining Sciences

journal homepage: www.elsevier.com/locate/ijrmms

Constraining the far-field in situ stress state near a deep South African gold mine

Amie M. Lucier [a,b,*], Mark D. Zoback [b], Vincent Heesakkers [c], Ze'ev Reches [c], Shaun K. Murphy [d]

[a] Shell International Exploration and Production, PO Box 481, Houston, Texas 77001-0481, USA
[b] Stanford University, Stanford, California
[c] University of Oklahoma, Norman, Oklahoma
[d] AngloGold Ashanti, South Africa

ARTICLE INFO

Article history:
Received 24 March 2008
Received in revised form
31 July 2008
Accepted 12 September 2008
Available online 13 November 2008

Keywords:
In situ stress
Mines
Breakouts
Drilling-induced tensile fractures
Boundary element modelling
Induced micro-seismicity

ABSTRACT

We present and test a new technique for determining the far-field virgin state of stress near the TauTona gold mine. The technique we used to constrain the far-field stress state follows an iterative forward modelling approach that combines observations of drilling-induced borehole failures in borehole images, boundary element modelling of the mining-induced stress perturbations, and forward modelling of borehole failures based on the results of the boundary element modelling. Using this approach, we constrained a range of principal stress orientations and magnitudes that are consistent with all the observed failures and other stress indicators. We found that the state of stress is a normal faulting regime ($S_{v^*} \geqslant S_{Hmax^*} \geqslant S_{hmin^*}$) with principal stress orientations that are slightly deviated from vertical and horizontal and, therefore, denoted with a (*). The maximum principal stress, S_{v^*}, is deviated $\sim 10^\circ$ from vertical plunging towards the NNW with a magnitude gradient of $\sim$27 MPa/km. The intermediate principal stress, S_{Hmax^*}, is inclined $\sim 10^\circ$ from horizontal plunging towards an azimuth of $\sim 156^\circ$ and has a magnitude gradient of $\sim$24 MPa/km. The least principal stress, S_{hmin^*}, is inclined $\sim 5^\circ$ from horizontal plunging towards an azimuth of 247° and has a magnitude gradient of $\sim$14 MPa/km. This stress state indicates that the crust is in a state of frictional faulting equilibrium, such that normal faulting is likely to occur on cohesionless pre-existing fault planes that are optimally oriented to the stress field. Modelling of breakout rotations and gaps in breakout occurrence associated with recent fault slip on critically stressed faults located >100 m from the mine further confirmed this stress state.

1. Introduction

As mining around the world moves deeper underground, understanding the stress field at depth, and how mining activity perturbs it, becomes increasingly important for mine safety. As a result of the mining-induced stress perturbations, deep underground mines tend to have appreciable mining-induced seismicity associated with them. Near the gold mines in the Witwatersrand Basin of South Africa, some of the deepest mines in the world, seismicity was first reported in 1908, about twenty years after the onset of gold mining in the region. Gane et al. [1] first directly associated the seismicity with the mining. Later, Gane et al. [2] established the close proximity of the event locations to the active mining faces. McGarr et al. [3] showed that most of the seismicity occurs in regions near the mining face with very large mining-induced stress perturbations. A more complete characterisation of the far-field stress will lead to better modelling of the mining-induced stress perturbations around the excavation. In turn, this can guide mining activities in the future and improve overall safety in the mines.

Constraining the far-field stress state is an important part of the Natural Earthquake Laboratory in South African Mines (NELSAM) project, which is working to develop a near-field laboratory to study earthquakes at seismogenic depths [4–6]. The deep gold mines of South Africa are unique locations for near-field studies of earthquake mechanics because of the high rate of mining-induced seismicity and the direct access to faults at seismogenic depths. However, the perturbation of the in situ stresses by the large-scale mining activities creates a complex stress field that complicates our understanding of the physical mechanisms controlling the induced seismicity. As part of the NELSAM project, we developed a new method to constrain the far-field in situ stress state surrounding the TauTona gold mine in the Western Deep Levels of the Witwatersrand Basin of South Africa.

Much of the previously published work on characterizing the far-field in situ stress state near the deep mines in the

* Corresponding author at: Shell International Exploration and Production, PO Box 481, Houston, TX77001-0481, USA. Tel.: +1 650 269 4597.
E-mail address: luciera@gmail.com (A.M. Lucier).

1365-1609/$ - see front matter © 2008 Elsevier Ltd. All rights reserved.
doi:10.1016/j.ijrmms.2008.09.005

Witwatersrand Basin relies on borehole strain relief measurements [7–9]. In their review of global stress measurements, McGarr and Gay [10] showed that in South Africa the stress state at depths below 2 km is typically a normal faulting stress regime, in which the vertical stress exceeds the horizontal stresses. These measurements also show that the minimum horizontal stress, S_{hmin}, magnitude is typically much lower than the vertical stress magnitude, S_v, although there was considerable scatter in the measurements.

In this study, we use both near- and far-field observations of stress indicators and boundary element modelling to constrain the far-field stress state and model the near-field perturbation of that stress state. The stress indicators used in the analysis are drilling-induced failures (i.e., breakouts and drilling-induced tensile fractures (DITFs)) observed in image logs from boreholes drilled within the mine at a variety of orientations. Peska and Zoback [11] discussed the mechanics controlling the formation of compressive and tensile failures in boreholes drilled at arbitrary orientations to principal stresses. These features have previously been used to constrain the stress states around oil and gas fields and other deep boreholes [e.g., 12]. Stacey and Wesseloo [13] review the use of these features for evaluating in situ stresses in deep mines. Because of the complexity of the stress perturbation around the mining excavation, the addition of boundary element modelling was necessary to analyse the drilling-induced failures observed in the near-field of the excavation. The technique we present follows an iterative forward modelling approach to constrain the far-field stress state that is consistent with the stress indicators observed in the near- and far-field to the mining excavation.

2. Data

2.1. Mine layout and rock properties

Because the mine excavations perturb the in situ stress state, a clear understanding of the geometry of the mine layout and the material properties of the in situ rock and backfill is critical. The geometry of the mine is illustrated in Fig. 1. The mining occurs along 0.5–1.5 m thick planar deposits of gold-bearing conglomerates, referred to as "reefs". In the TauTona mine, the Carbon Leader Reef is mined; in the shallower Mponeng mine (red), which overlaps TauTona towards the southwest, the Ventersdorp Contact Reef is mined. The bedding dips about 20° towards the SSE.

The NELSAM study area is located in the tunnels below the stope in the southeastern part of the mine. The reef in this region is offset by the Pretorius Fault Zone (PFZ), an ancient normal to strike-slip fault zone that dips steeply and strikes approximately NE-SW. This is an area of active mining and is near the deepest part of the mine at a depth of approximately 3.6 km. In Fig. 1d, the active mining region is categorized into three mining steps (1, 2, and 3) that represent the extent of mining at June 2005, January 2006, and June 2006, respectively. These correspond to the times at which borehole drilling and image logging occurred. The access tunnels have a more localised effect (out to ~2 tunnel

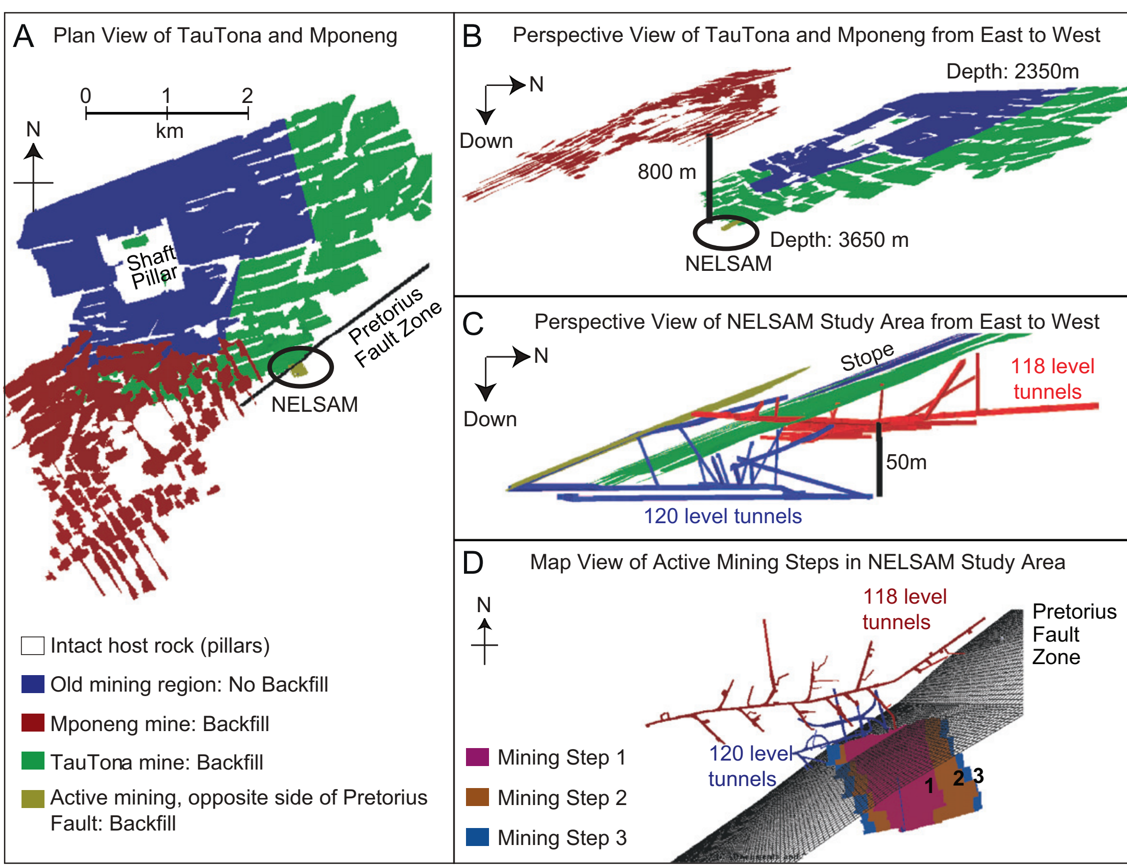

Fig. 1. Layout of the mine. (A) Plan view of the stope of Mponeng mine (red) and TauTona mine (blue, green, and yellow) and the PFZ (black). The white area represents the intact host rock and the colour regions indicate the area that has been mined. The NELSAM study area is in the southeastern part of TauTona. (B) Perspective view of the stope from the east without the PFZ. The NELSAM study area is located in the deepest part of the mine. Mponeng is about 800 m shallower than TauTona. (C) Zoomed in perspective view of the NELSAM study area from the east. The active mining (yellow) is offset from the older mining (green) by displacement along the PFZ. The 118 and 120 level tunnels are also shown; they are separated by 50–60 m. (D) Map view of the NELSAM study area tunnels, the PFZ, and the active mining section, which is broken into three mining steps. The older mining region (green) of the stope is not shown so that the tunnels are visible.

radii) on the stress state than the stope. Therefore, for the purpose of this work, they are only modelled in the NELSAM area where borehole logging was carried out as shown in Figs. 1c and d and 2.

The intact host rock is primarily quartzite. The average material properties for the host rock used in the modelling include a uniaxial compressive strength of 200 MPa, Poisson's ratio of 0.20 and a Young's modulus of 70 GPa, as based on laboratory measurements [14,15]. These values have been used in previous studies in TauTona [16]. In Fig. 1, the green and yellow regions represent backfilled excavations in TauTona and the red represents the backfilled excavation in Mponeng. The backfill is a slurry of waste material that is pumped back into the excavation to provide support. The material properties of the backfill in TauTona and Mponeng were provided by the mine engineers and are calibrated based on previous modelling by the mining engineers (Shaun Murphy, personal communication). The backfill materials have no cohesion or tensile strength and a friction angle of 10°. The Mponeng backfill has a shear modulus of 10 MPa and a normal modulus of 16 MPa and TauTona backfill has a shear modulus of 14.4 MPa and a normal modulus of 14.4 MPa. The shear and normal moduli relate the elastic shear and normal displacements and the shear and normal stresses acting on the material.

2.2. Borehole camera image logs

Borehole image logs provide oriented images of the walls of the boreholes. Drilling-induced borehole failures such as DITFs and borehole breakouts as well as natural fractures that intersect the boreholes can be observed in these image logs. In this work, image logs were collected in six 6.6–11.5 m vertical boreholes (sites 2 and 3 in the 118 level and sites 7 V, 9, 10, and 13 in the 120 level), five 9.6–39-m long boreholes deviated 43–80° from vertical (3 boreholes at site DAF in the 118 level and site 7 N and 7 S in the 120 level), and in the long subhorizontal LIC118 borehole in the 118 level (Fig. 2). The LIC118 borehole is deviated 70–85° from vertical towards the east and 418 m of image log data were collected. Logging at sites 10, 13, and LIC118 corresponds to mining step one (June 2005), logging at sites 9 and DAF 1 corresponds to mining step two (January 2006), and logging at sites 2, 3, 7, and DAF 5 and DAF BIO corresponds to mining step

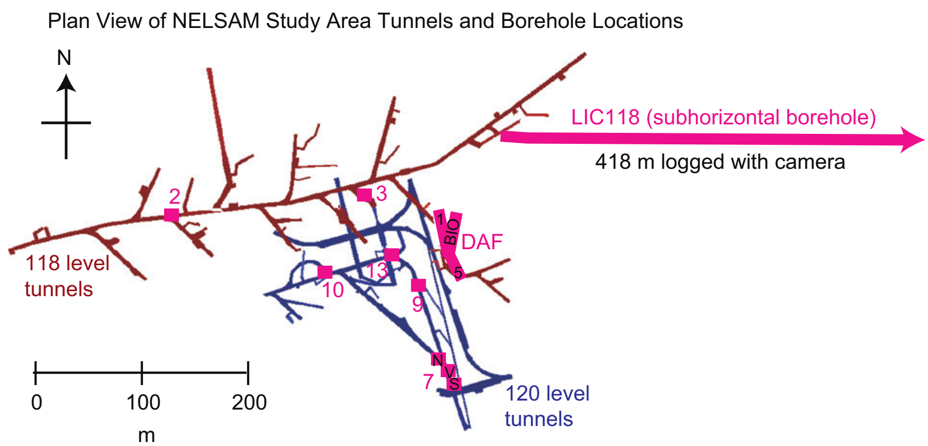

Fig. 2. Locations of boreholes logged in the 118 and 120 level tunnel systems. Sites 2, 3, 7V, 9, 10, and 13 are vertical boreholes. The three boreholes at the DAF site (1, 5, and BIO) and two boreholes at site 7 (N, S) are deviated. The LIC118 borehole is sub-horizontal and extends away from the mining into the far-field.

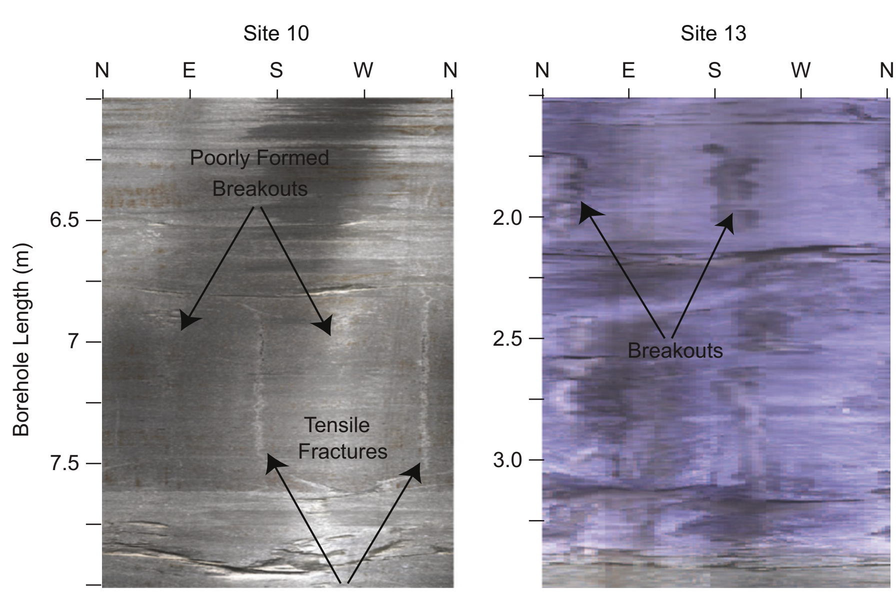

Fig. 3. Example borehole image logs from sites 10 and 13. Images are shown in an unwrapped borehole view and are oriented with north on the sides of the images and south in the centre of the images. The site 10 image illustrates DITFs and poorly formed breakouts, while site 13 shows breakouts.

three (June 2006). Fig. 3 shows examples of drilling-induced failures observed in the image logs.

2.3. Overcoring measurements

In February 2000, two in situ stress measurements were completed within the shaft pillar using the overcoring technique and reported in an internal report [14]. These tests were carried out in the roof of a tunnel in the shaft pillar area at the 83 level (2361 m deep). The measurements were about 10.5 m into the access boreholes. The maximum principal stress (S_1) was deviated about 20° from vertical plunging towards the NNW. The magnitude gradient of S_1 was about 36 MPa/km which is significantly higher than the predicted vertical stress gradient of 27 MPa/km based on an average overburden density of 2700 kg/m^3. This is likely due to the stress concentration in the shaft pillar which is supporting the excess vertical load resulting from the excavation of the stope. The intermediate principal stress (S_2) was deviated about 20° down from the horizontal towards the SSE and had a magnitude gradient of about 19 MPa/km. The minimum principal stress (S_3) was nearly horizontal in the WSW direction with a gradient of about 10 MPa/km. Therefore, the nearly horizontal principal stress components in the shaft pillar region are significantly anisotropic. These measurements are generally consistent with the normal faulting stress state for South Africa reported by McGarr and Gay [10].

3. Methodology for constraining the far-field stresses

We followed an iterative forward modelling approach to characterize the far-field in situ stress state near TauTona mine (Fig. 4). Each step of the workflow is described in the following sections. The final result was to constrain the range of principal stress orientations and magnitudes that are consistent with all the observed data.

3.1. Borehole data analysis

The first step of the workflow is to analyse and document the drilling-induced failures observed in the borehole image logs. The results of this analysis are summarised in Table 1. Site 10 was the only borehole where both DITFs and breakouts were observed, although the breakouts were poorly formed. Site 13 and LIC118 boreholes both had breakouts. Two of the boreholes at the DAF site (5 and BIO) and the vertical borehole at site 7 (V) had DITFs. In some of the boreholes, no drilling-induced failures were observed. The image log collected in borehole 1 at the DAF site was of poor quality and could not be analysed.

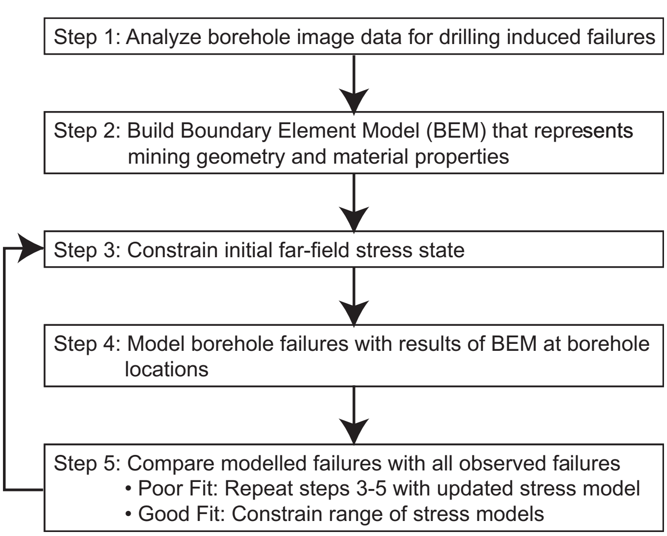

Fig. 4. Iterative forward modelling workflow for constraining in situ far-field stresses.

The LIC118 borehole was of particular importance for this analysis, because it was drilled into the far-field stress state away from the mining excavation. Breakouts occurred starting at a measured depth of 35 m and were observed throughout the length of the borehole (Fig. 5). A large-scale rotation in the position of the breakouts around the borehole walls occurred between 35 and about 150 m measured depth. From 150 m to the end of the borehole, the breakout positions and widths were relatively consistent, confirming that the borehole is extending into the far-field stress state. The breakouts formed on the sides of the borehole suggesting a vertically oriented maximum compression. Localised rotations in the breakout position as well as gaps in breakout occurrence were also observed throughout the length of the borehole image log.

3.2. Building boundary element model

A boundary element modelling program Map3D [17], which was developed for mining applications, was used to numerically model the response of the rock to the mining activity. Map3D is based on an indirect boundary element method. The program has been used to examine the stress perturbation from mining and the associated failure in several mine settings [e.g., 18–20]. The model accounts for the geometry of the stope and access tunnels, the structural support provided by backfill materials, and the stress loading conditions applied by the far-field in situ stress state. The model simulates the rock mass response to these inputs while honouring the physical constraints of equilibrium, continuity, and elasticity. The model space begins as a homogeneous, elastic medium that approximates the in situ host rock; therefore, far-field boundary conditions are accommodated. The mining excavation and access tunnel are then incorporated as elements and the response to these elements is calculated on specified grids.

The mine geometry shown in Fig. 1 was modelled with two types of elements referred to as *fictitious forces* and *displacement discontinuities*. Because the access tunnels in the NELSAM study area are void spaces, they were modelled as fictitious force elements that have zero surface stresses. The stope was modelled with displacement discontinuity elements which had material property values corresponding to the appropriate backfill materials modelled with an elasto–plastic constitutive law.

The stress state at each borehole needed to be analysed based on the extent of the mining at the time of the camera logging. This corresponds to three mining steps: June 2005, January 2006, and June 2006 (Fig. 1d). The BEM simulates the stress perturbations after each of these mining steps and calculates the results on specified grids (at the borehole locations, on planes of interest near the boreholes, and along mapped fault planes) within the model.

3.3. Initial far-field stress model estimate

The goal of the workflow is to constrain the far-field stress state that is consistent with the observed stress indicators. To do this, we first estimate a far-field stress model to be used as the initial condition to solve for the mining-induced stress perturbations with the BEM. This model defines the principal stress orientations and magnitudes and pore pressure, and it provides a

Table 1
Borehole observations of breakouts and DITFs

Borehole	Tunnel level	Borehole trajectory	Length (m)	Drilling-induced failure observations	Image quality
Site 2	118	Vertical	7.1	No failures observed	Good
Site 3	118	Vertical	8.5	No failures observed	Good
Site 7N	120	Dev: 47° Azi: 142°	10.5	No failures observed	Fair
Site 7V	120	Vertical	9.4	DITF: 6 m: position 222°, inclination 10° 8 m: position 198°, inclination 1° 9 m: position 170°, inclination 179°	Good
Site 7S	120	Dev: 43° Azi: 322°	9.6	Low-quality data, no clear evidence for failures	Poor
Site 9	120	Vertical	11.4	No failures observed	Good
Site 10	120	Vertical	11.5	DITF: 6 m: position 161 °, inclination 12° 9 m: position 152 °, inclination 160 ° Breakouts: Poorly formed, position 62°,width 20°	Good
Site 13	120	Vertical	6.6	Breakouts: Well formed, some localized rotation Position 55–65°,width 40°	Good
DAF 2	118	Dev: 110° (20° up from horizontal) Azi: ~346°	39	Low-quality data	Poor
DAF 5	118	Dev: 70° Azi: ~156°	19	DITF: 5 m: position 90°, inclination 15° 15 m: position 105°, inclination 176°	Good
DAF BIO	118	Dev: 110° (20° up from horizontal) Azi: ~353°	37.9	Low-quality data DITF Evidence from 5 to 10 m: Position: 145–170°, Inclination 30°	Poor–fair
LIC118	118	Dev: 75–85° Azi: ~90°	418 (logged)	Breakouts along extent of borehole, see Figs. 4–6	Fair–good

For borehole trajectory, Dev is deviation from vertical and Azi is borehole azimuth.

starting point for the iterative forward modelling used to constrain the stress model.

3.3.1. *Stress regime*

We initially assumed that the principal stresses were oriented vertically (S_v) and horizontally (S_{Hmax} and S_{hmin}). While this is a simple assumption, it is often observed in stable cratonic crust [21] around the world. We also assumed a normal faulting stress regime such that $S_v \geqslant S_{Hmax} \geqslant S_{hmin}$. This was based on the observations of McGarr and Gay [10], the overcoring measurements, and the position of the breakouts observed in the LIC118 borehole.

3.3.2. *Horizontal stress orientations*

We used information from the overcoring stress measurements and the drilling-induced failures observed in the vertical boreholes as an initial estimate the orientations of the horizontal stresses. The overcoring measurements indicated an S_{Hmax} azimuth of 153° [14]. The DITFs at site 10 suggest an S_{Hmax} azimuth of 158° and the breakouts observed at site 13 borehole suggest an S_{Hmax} azimuth of 155°. Based on these three consistent observations, we chose an initial S_{Hmax} orientation of 155° and an orthogonal S_{hmin} azimuth of 245°.

3.3.3. *Vertical stress magnitude*

The initial S_v magnitude results from the weight of the overburden material. The average density of the overburden at TauTona was estimated to be 2700 kg/m^3. By integrating the density over the depth of the mine, the average S_v gradient was estimated to be 27 MPa/km.

3.3.4. *Pore pressure*

No direct measurements of the pore pressure, P_p, have been made in or around the mine. Furthermore, the dewatering of the area directly around the mine makes P_p difficult to quantify. Within the mine, P_p is considered to be negligible. However, given the low permeability of the rocks in TauTona (~10^{-20} m^2), the diffusion rates are on the order of 30 m over 10 years or 70 m over 50 years [22]. Based on these rates, we estimated that the influence of the dewatering extends about 100 m away from the mine. Previous studies have shown that hydrostatic P_p is observed around the world in deep boreholes, even those in low porosity (<2%) and very-low permeability crystalline rocks [22–24]. Therefore, it was assumed that the far-field virgin stress state has hydrostatic despite the dewatering and general dryness observed in the mine.

3.3.5. *S_{hmin} magnitude*

Breakout rotations and gaps in breakout occurrence were observed throughout the length of the LIC118 borehole image log. Previous studies have shown that these features in the observed breakouts are associated with recent slip on faults [25,26]. This suggests that the far-field stress state around the mine is likely to be critically stressed (i.e., faults which are well-oriented to the stress field are near the point of frictional slip). Thus, frictional faulting theory could be used to constrain the maximum difference between the vertical principal stress magnitude (S_1 in normal faulting areas) and the minimum principal stress magnitude, S_3 [12]. In frictional faulting theory, the ratio of the maximum effective stress (σ_1) to the minimum effective stress (σ_3) is controlled by the coefficient of friction (μ) of optimally oriented faults in the crust.

$$\frac{S_1 - P_p}{S_3 - P_p} = \frac{\sigma_1}{\sigma_3} = (\sqrt{\mu^2 + 1} + \mu)^2 \tag{1}$$

This equation defines the upper limit for the σ_1/σ_3 ratio. The general range for μ observed in the brittle upper crust is 0.6–1.0 [27,28]. Solving for S_3 in Eq. (1) using $\mu = 1$ predicts the lower bound for S_3 to be 13 MPa/km ($S_1 = 27$ MPa/km, $P_p = 10$ MPa/km).

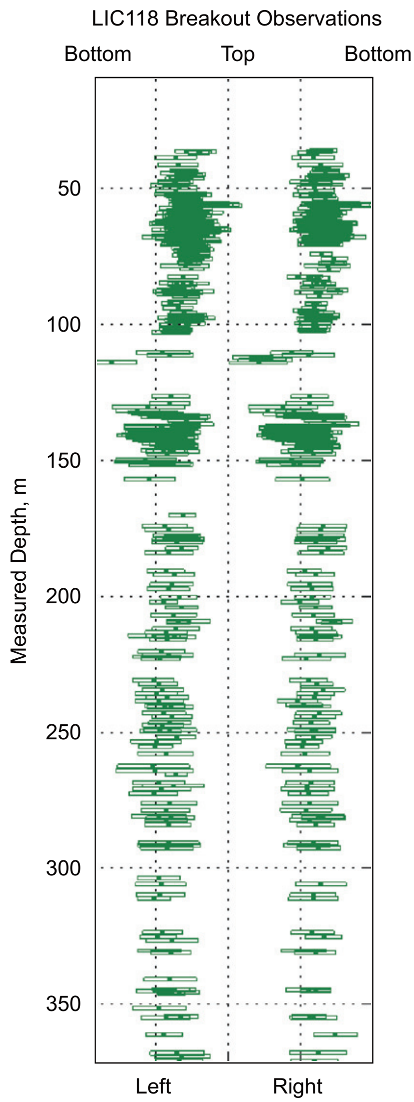

Fig. 5. Breakout observations in the LIC118 borehole. These are shown as an "unwrapped" borehole wall, with angle around the hole plotted with measured depth. Breakout positions are plotted in a borehole reference frame that is relative to the bottom of the borehole looking down the borehole. The widths of the breakouts are also indicated.

3.3.6. S_{Hmax} magnitude

Observations from the overcoring measurements and the DITFs observed in the site 10 borehole were used to estimate the magnitude of the intermediate stress, S_{Hmax}. The minimum and maximum horizontal stress magnitudes measured from overcoring differ by nearly a factor of two. Likewise, the presence of DITFs at site 10 suggested significant horizontal stress anisotropy [12]. Therefore, the initial S_{Hmax} gradient was estimated to be 26 MPa/km, which is twice that of S_{hmin} but slightly less than S_{v}.

In summary, the initial far-field stress state model was a normal faulting regime with S_{v}, S_{Hmax}, S_{hmin}, and P_{p} gradients of 27, 26, 13, and 10 MPa/km, respectively. The S_{Hmax} azimuth is 155° and the S_{hmin} azimuth is 245°. While these stress magnitudes and orientations provided a reasonable starting point for the far-field stress model, as discussed below, each of them was subject to revision based on the results of steps 4 and 5 of the workflow.

3.4. Modelling borehole failure with BEM results

Drilling-induced borehole failures result from the concentration of the effective stresses around the borehole walls during and after drilling. The position and width of the drilling-induced failures (and angle of inclination for the case of en echelon DITFs) depends on the relative orientations of the borehole and the principal stresses [11]. Breakouts form when the stress concentration at the borehole wall exceeds the rock strength. DITFs form when the tensile stress concentration at the wellbore wall is less than the tensile strength of the rock. In a vertical borehole with principal stresses oriented vertically and horizontally, breakouts form in the direction of S_{hmin} and DITFs form in the S_{Hmax} direction. However, when the borehole and/or the principal stress orientations are deviated from vertical, there is no simple relationship between the stress orientations and the position around the borehole at which the drilling-induced failures will occur [11].

In this study, we used a forward modelling tensor transformation technique to model failures, because for all the cases the boreholes and/or stress field were deviated from vertical. The mining-perturbed principal stress magnitudes and orientations at locations along the boreholes were solved for using the BEM. The far-field stress model from step 3 provided the initial conditions for the model. Using the (1) mining-perturbed stresses at the borehole locations, (2) borehole orientations, and (3) rock properties, the expected borehole failures were predicted. The results of both the BEM calculation using the initial far-field stress model and the breakout modelling based on those results are shown for the LIC118 borehole in Fig. 6.

3.5. Comparing borehole failure observations with modelling results

The final step in the methodology is to compare the borehole failures modelled in the previous step to the observed borehole failures in the image logs in all of the boreholes (Table 1). If the modelled failures were not consistent with the observed failures (based on a qualitative comparison), then the far-field stress model used in the BEM was not considered within the range of acceptable models. The results from the LIC118 borehole had the most weight, because these were less dependent on the details of the boundary element model and they sample the far-field stress state. Overall, the modelled breakouts for LIC118 using the initial far-field stress model were consistent with the observed breakouts, although the modelling did not predict the absence of breakouts at the beginning of the borehole (Fig. 6b).

In the other boreholes, the modelled failures using the initial model were mostly consistent with the observations. In sites 2, 7N, and 9, where no failures were observed, the modelling predicted no failures. However, at sites 3 and 7S, where no failures were observed, the modelling predicted the formation of DITFs at the beginning of the boreholes. Breakouts and DITFs were modelled at site 10 in the observed orientations, but the breakouts at both sites 10 and 13 were modelled with larger than the observed widths. At site 7 V, the modelled DITFs were consistent with the observations. However, breakouts were modelled although they were not observed in the borehole. In both the BIO and the boreholes at the DAF site, DITFs were modelled and observed.

The initial stress model provided a good starting point for the analysis. To determine the range of stress models consistent with the observations, steps 3–5 in the methodology (Fig. 4) were repeated by systematically testing each of the assumptions used to constrain the initial stress state model. Because of the nature of the borehole image data, the limitations of the boundary element

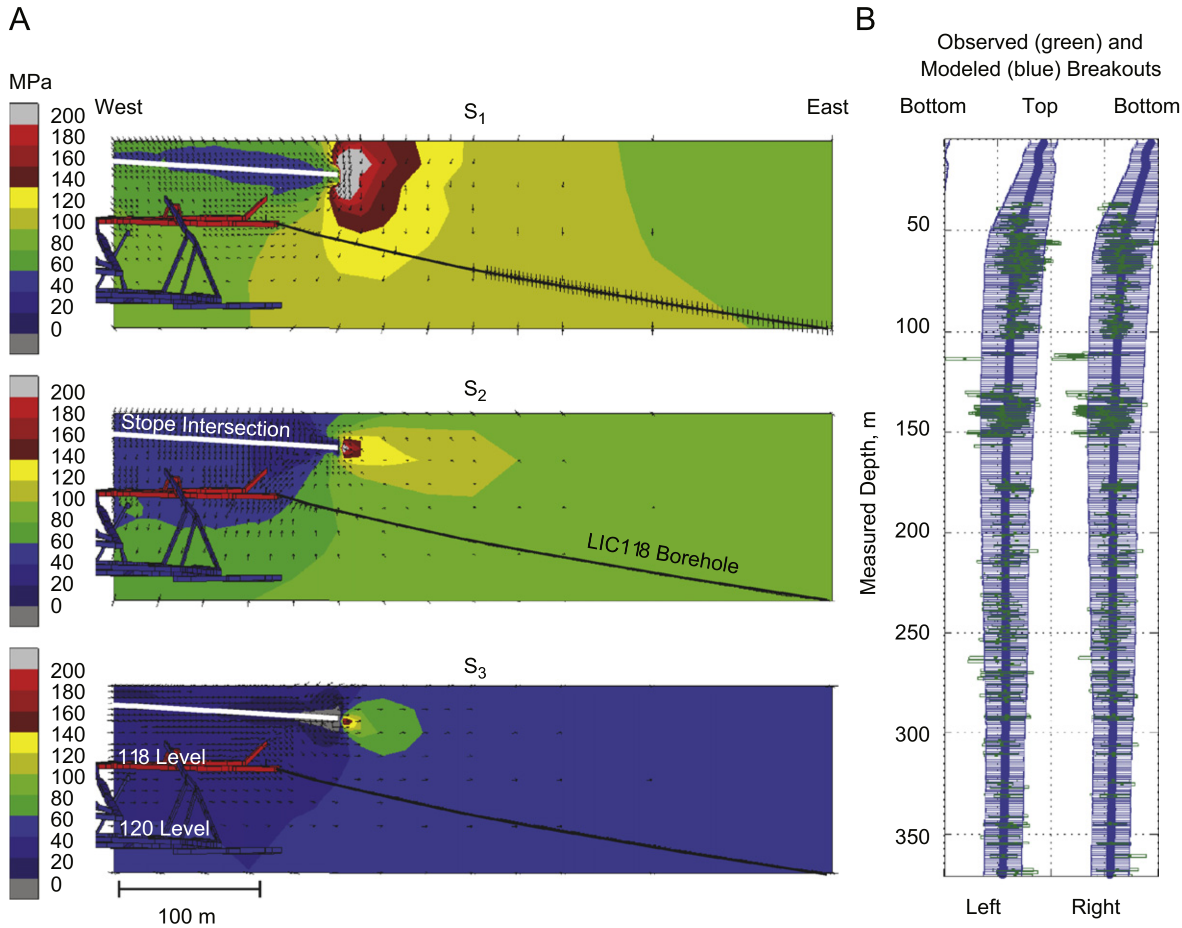

Fig. 6. Boundary element modelling results based on the initial far-field stress model. (A) Principal stress orientations (arrows) and magnitudes (colour scale) along a vertical plane extending from the LIC118 borehole trajectory. The intersection of the plane and the stope is shown by a white line. The 118 (red) and 120 (blue) tunnels are shown for reference. (B) Observed (green) and modelled (blue) breakouts along the LIC118 borehole. The data is plotted in a borehole reference frame looking down hole.

modelling, and the forward modelling approach, the solution to the far-field stress will be non-unique. The goal of this work was to constrain the range of stress models over which the modelled borehole failures were consistent with the observations.

4. Results

The initial estimate of the far-field stress state was updated by testing the main assumptions used to constrain it. These assumptions were: (1) normal faulting stress regime with vertical and horizontal principal stresses, (2) horizontal stress orientations, (3) S_v magnitude, (4) P_p magnitude, (5) S_{hmin} magnitude, and (6) S_{Hmax} magnitude. The details of these tests are summarised in Appendix A. This analysis resulted in a well-constrained stress model for the region around the TauTona gold mine which is described below.

The resulting stress model suggests that the crust around TauTona is critically stressed, such that the stress magnitudes are constrained by frictional failure equilibrium theory and small stress perturbations may lead pre-existing, optimally oriented faults into failure. We provide further evidence that supports a critically stressed crust by modelling the localised rotations and gaps in the occurrence of breakouts observed along the LIC118 image log. We show that these features are associated with faults that are optimally oriented for recent slip.

4.1. Far-field stress model

We constrained the range of far-field stress models that were consistent with the observed data in both the near- and far-field of the mining excavation. The far-field stress model is summarised in Fig. 7. The magnitudes of the principal stresses are plotted with depth in Fig. 7a and the range of principal stress orientations are shown in the green shaded regions of Fig. 7b. The state of stress is a normal faulting regime $(S_{v^*} > S_{Hmax^*} > S_{hmin^*})$ with principal stress orientations that are slightly deviated from vertical and horizontal and, therefore, denoted with a (*). The maximum principal stress, S_{v^*}, is deviated 0–20° from vertical plunging towards the NNW and has a magnitude gradient ranging from 26.7 to 27.3 MPa/km. The intermediate principal stress, S_{Hmax^*}, is inclined 0–20° from horizontal plunging towards an azimuth between 145° and 168° and has a range in magnitude gradient between 21 and 26 MPa/km. The least principal stress, S_{hmin^*}, is inclined 0–10° down from horizontal towards an azimuth between 235° and 258° and has a magnitude gradient ranging from 12.9 to 15.5 MPa/km. A representative far-field stress model is shown by the symbols in Fig. 7. The principal stress magnitude gradients are 27.2, 24, and 14 MPa/km; and principal stress orientations are an S_{v^*} azimuth of 345° and plunge of 80°, an S_{Hmax^*} azimuth of 157° and plunge of 10°, and a nearly horizontal S_{hmin^*} with an azimuth of 247°. This stress model was chosen to investigate critically stressed faults in the vicinity of the mine.

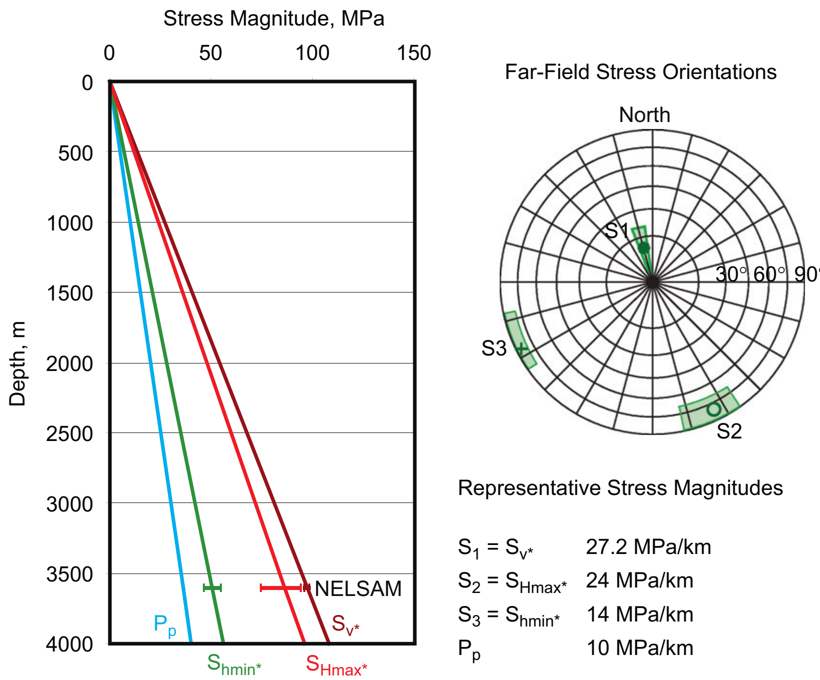

Fig. 7. Constrained far-field stress model. On the left, the representative principal stress magnitude and P_p gradients (as described on the bottom right) are shown in a pressure versus depth plot. At the depth of the NELSAM study area, the acceptable ranges in stress magnitudes are illustrated with error bars. On the right, a stereonet plot shows the range in acceptable principal stress orientations in the green-shaded regions and the representative stress model orientations with the green symbols.

4.2. *Critically stressed crust*

The far-field state of stress around TauTona is in frictional faulting equilibrium as predicted by Mohr-Coulomb failure criterion, such that the crust is in a constant state of frictional failure along optimally oriented, cohesionless, pre-existing faults (Fig. 8). While the rate of the brittle deformation in shield areas like the Kaapvaal Craton of South Africa is quite slow as compared to most intraplate regions, well-oriented faults are still critically stressed [29]. This frictional failure results in stress drops that limit the stress magnitudes that can be sustained in the crust. A fault plane is optimally oriented, or critically stressed, when the Coulomb failure function (CFF) resolved on the fault is positive. This occurs when the shear stress (τ) resolved on the fault plane is greater than the product of the effective normal stress ($S_n - P_p$, where S_n is normal stress) and μ along the fault plane.

$$\mathrm{CFF} = \tau - \mu(S_n - P_p) \tag{2}$$

Faults dipping 50–85° to the ENE or WSW are critically stressed in the far-field stress state (Fig. 8).

The critically stressed crust near TauTona is supported by observations of localised breakout rotations and gaps in breakout occurrence along the LIC118 borehole (Fig. 5). Previous work has shown that localised rotations in the position of breakouts and interruptions in breakout formation are associated with stress perturbations from recent slip on nearby faults [25,26]. To determine if these breakout observations were consistent with the constrained stress state, we examined if they could be explained by slip on the natural faults observed in the LIC118 image logs. First, natural faults corresponding to local breakout rotations or gaps in the occurrence of breakouts were identified in the image log. Then, we determined whether the fault orientations were critically stressed (i.e., CFF$>$0) in either the virgin (i.e., representative stress state defined above) or mining-perturbed stress state (from BEM calculation). For a critically

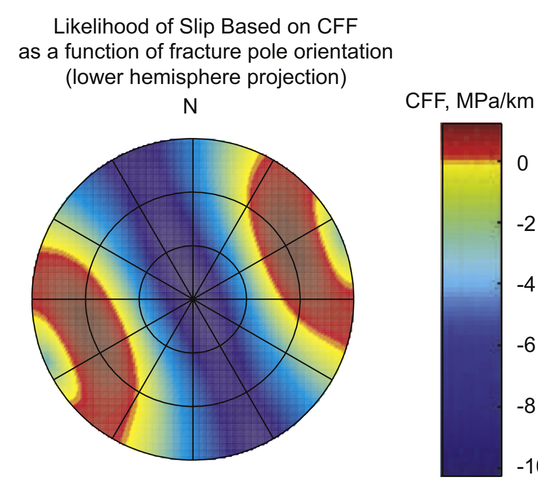

Fig. 8. Lower hemisphere projection stereonet plot of Coulomb failure function (CFF) for fracture plane poles in the far-field stress model. Red colours indicate pole orientations that are critically stressed (positive CFF). Normal faults striking SSE and NNW are critically stressed. Analysis assume $\mu = 0.6$ and zero cohesion along the fault surfaces.

stressed fault, we predicted the breakout formation expected as a result of the orientation of the borehole relative to the stress field, which has been perturbed by both the mining and slip on the fault.

We followed the methodology proposed by Barton and Zoback [25] to analyse the breakout rotations and gaps with respect to the critically stressed faults. First, the local perturbation of the stress field due to slip on the critically stressed fault was modelled. This required the determination of the slip vector on the fault. The slip direction is the direction of maximum shear stress (τ) resolved on the fault plane, which is a function of the fault orientation and the mining-induced stress state at the fault location as described by Keilis-Borok [30] for a fault patch of dimensions $2L \times 2L$ in Eq. (3).

$$d = \Delta\tau_s \frac{16}{7\pi G}\frac{2L}{\sqrt{\pi}} \tag{3}$$

The magnitude of the slip vector, d, depends on the fault patch size, the shear modulus of the faulted material, G, and the stress drop, $\Delta\tau_s$. Shamir and Zoback [26] showed that the size of the slip patch is on the order of the size of the anomaly of the breakout formation. The magnitude of $\Delta\tau_s$ is a percentage of the available shear stress in the slip direction and controls the magnitude of the anomaly. Next, the breakout formation around the faults was modelled based on the combined effects of the fault-perturbed stress field, mining-perturbed stress field, borehole trajectory, drilling conditions, and rock properties including rock strength and Young's.

Fig. 9 shows two examples of the breakout modelling analysis for faults that become critically stressed due to the mining-induced stress changes. Because the faults have become critically stressed due to the recent mining-induced stress perturbations, it is likely that any slip on these faults occurred recently. In the first example, we examined a fault which strikes 115° and dips 78° and corresponds to a localised rotation in breakout position at about 131 m measured depth in the LIC118 borehole (Fig. 9A). Based on the length of the breakout rotation, we estimated a square fault patch of 64 m^2 centred on the borehole. Slip on a fault of this size and orientation in the mining-perturbed stress field would have a

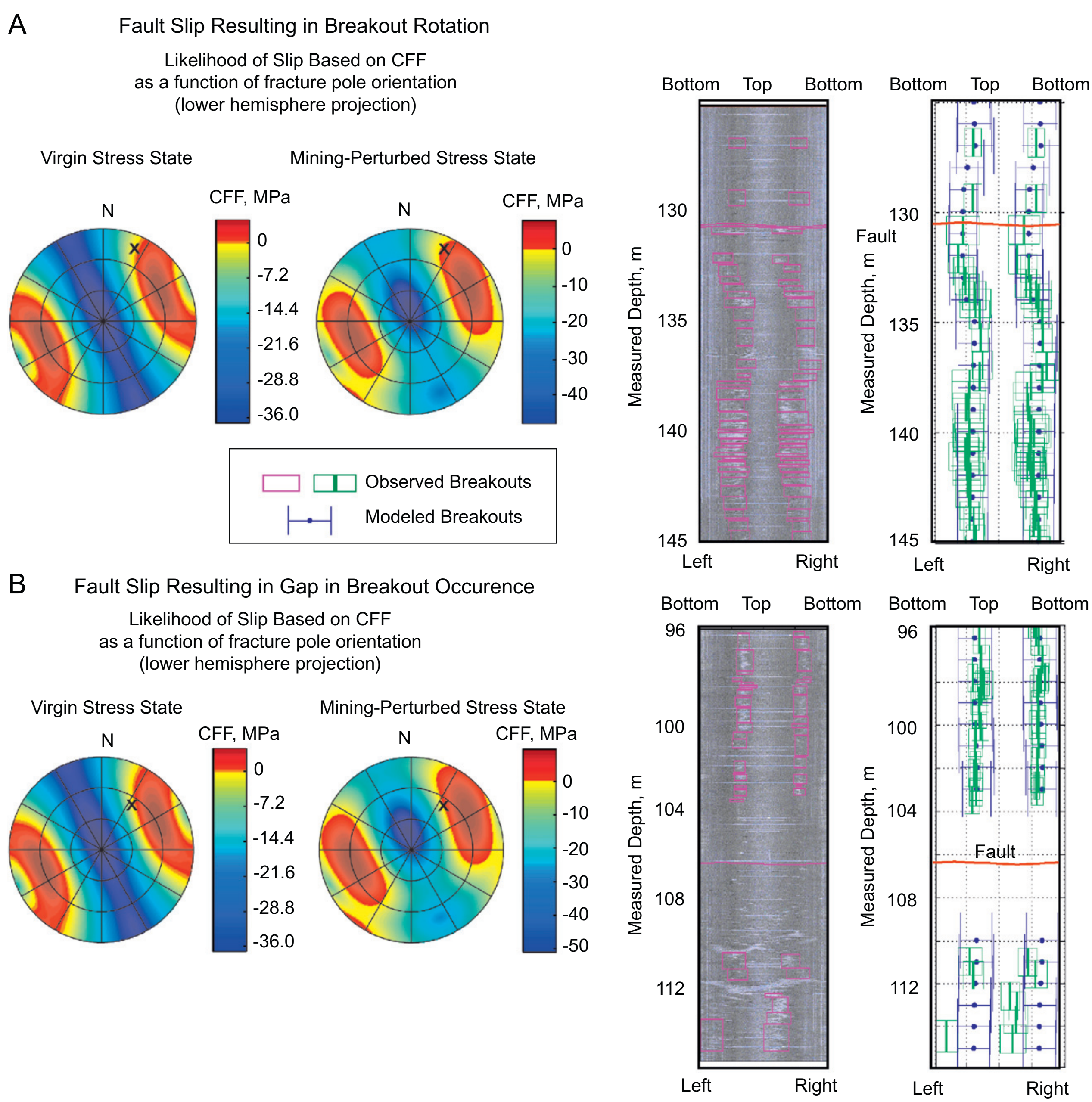

Fig. 9. Two examples of modelling breakouts near critically stressed faults. (A) Modelling fault slip that resulted in a rotation in the breakout position. On the left, fault plane poles are plotted on a lower hemisphere stereonet and colour coded with CFF for both the virgin and mining-perturbed stress fields at the fault location. The analysed fault orientation is indicated by the black X. The right centre panel shows the borehole image log data and interpretation of the fault and breakouts. The data is shown as an unwrapped borehole in a reference frame of looking down the borehole. The right panel compares the observed breakouts (green) with the modelled breakouts (blue). The fault is shown in red (red). (B) Modelling slip on a fault that resulted in a gap in breakout occurrence. The panels are the same as described for A.

rake of 43.3° and 6.3 mm of dislocation. Assuming a complete stress drop, the stress relief would be 23.4 MPa. Based on this fault perturbed stress field, the predicted breakout formation closely matched the observed local breakout rotation.

In Fig. 9B, we illustrate that slip on critically stressed faults observed in the LIC118 borehole image log can also be associated with the gaps in breakout. A fault striking 126° and dipping 53° was observed at 106.4 m measured depth. The local stress perturbation associated with slip on a 100 m^2 square fault patch of that orientation (i.e., 11.4 mm of slip with a rake of 58.9°) centred on the borehole with a complete stress drop (33.6 MPa) resulted in a gap in the formation of breakouts around it. This was consistent with the breakout observations at that depth, providing further support for the far-field state of stress that was constrained in this work.

5. Conclusions and recommendations

The state of stress around TauTona was determined to be in a normal faulting regime with ENE and WSW dipping normal faults being critically stressed. Because the stress state is critically stressed, stress perturbations, such as those associated with the stope excavation, can reactivate faults at orientations that were previously stable. The implications of this are currently being investigated with respect to specific faults observed in the mine.

The workflow developed in this paper combines elements of techniques that are used to constrain stresses in deep boreholes and oil and gas wells [12] along with boundary element modelling to constrain the far-field stresses near a deep underground mine. Without the BEM, the data collected in the near-field boreholes could not be effectively interpreted, therefore, the incorporation of the BEM calculations of the mining-induced stress perturbation is an essential step in this workflow. The implementation of the workflow in this study also indicates ways in which it could be improved upon. Although, we recognise that there are a number of operational and financial constraints of working in an active mine. First, one or more long boreholes that extend into the far-field stress state must be logged with a borehole camera to assess borehole failures in the virgin stress field. Increasing the number of boreholes that reach the far-field with different borehole trajectories will result in a more well-constrained stress model. In the near-field to the excavation, logging of vertical boreholes is preferable to deviated boreholes both for the ease of data acquisition and data analysis. These boreholes should be at least 10 m long (although longer boreholes are preferred) and located away from complicated tunnel intersections. The optimal locations of the boreholes should be chosen based on preliminary BEM results. Boreholes should be located where there is minimal complexity of the mining perturbed stress state and where the mining-perturbed stress state is likely to result in borehole failures. Our final recommendation is that P_p and the S_3 magnitude should be measured in the boreholes that reach the far-field. The S_3 magnitude can be measured with minifrac tests, which are commonly used in oil and gas wells. Having a measurement of S_3 would decrease the number of assumptions that are needed to constrain the stress state and would result in a more precisely constrained far-field stress state.

Acknowledgments

This work was made possible, thanks to invaluable help by Hannes Moller, Pieter van Zyl, and many underground workers in TauTona mine of AngloGoldAshanti. We would like to thank Gerrie van Asegen and Gerhard Hofmann of ISS International for their help with Map3D. Thanks to AngloGoldAshanti for the permission to use the TauTona mine data for the modelling. This work is supported by the National Science Foundation under Grant no. 0409605 (NELSAM). Any opinions, findings, and conclusions or recommendations expressed in this material are those of the author(s) and do not necessarily reflect the views of the National Science Foundation. Other sponsors of this work include Inter-Continental Drilling Program (ICDP), AngloGoldAshanti, ISS International, and National Research Foundation (NRF).

Appendix A

Section 3.3 outlines the assumptions used to estimate the initial far-field stress state which defines the initial conditions for the BEM calculations. To constrain the range in far-field stress states consistent with the observed data, the limits of these assumptions were systematically tested by repeating steps 3–5 of the workflow (Fig. 4). The limits of the horizontal stress magnitudes tested were constrained by frictional failure theory. For a specified S_{v^*}, P_p, and μ, the frictional failure limits for both S_{Hmax^*} and S_{hmin^*} can be defined using a "constrain stress" polygon [31] (Fig. A1a). The "stress space" defined by the polygons limits the range of stress magnitudes that were tested for validity in this analysis (Fig. A1a).

Fig. A1b shows the region of the stress polygon that represents a normal faulting (NF) regime. The combinations of horizontal stress magnitudes tested in this analysis are labelled numerically 1 though 8. In Fig. A1c, the stress orientations used in some of the models are labelled alphabetically A through D. We refer to the models in terms of these labels. For example, the initial stress model which has the magnitudes summarised by the blue circle labelled (1) in Fig. A1b and the orientations of the blue symbols labelled A in Fig. A1c is called model 1A. The assumptions that were tested are: (1) normal faulting stress regime with vertical and horizontal principal stresses, (2) horizontal stress orientations, (3) S_v magnitude, (4) P_p magnitude, (5) S_{hmin} magnitude, and (6) S_{Hmax} magnitude.

A.1. Stress regime

The first assumption for the initial stress model was that the principal stresses are oriented vertically and horizontally and the vertical stress is greater than the horizontal stresses. To test whether the stresses are aligned vertically and horizontally, we analysed stress models with the stress magnitude parameters of 2 (Fig. A1b) and with the vertical stress deviated 10°, 15°, and 20° from vertical. First, S_v was deviated from vertical towards an azimuth of 345° (the azimuth of S_1 from the overcoring measurements). The S_2 azimuth was fixed at 155°, but the S_2 inclination angle and S_3 orientation were adjusted as S_1 was deviated to maintain the orthogonal nature of the principal stresses. As the deviation angle increased, the breakout positions modelled in the far-field of the LIC118 borehole-rotated clockwise around the borehole wall (looking down the borehole). The predicted breakouts from the initial stress model were centred at 97–277° from the bottom of the hole. For a stress state with S_v deviated 20° to the NNW, the breakouts were predicted at 108–288° from the bottom. The observed breakouts are centred at approximately 105–285°. Therefore, the deviation of S_1 from vertical towards the NNW resulted in a more consistent fit to the observed breakouts in the LIC118 borehole and had little to no effect on the failures modelled in the shorter boreholes in the near-field of the mining.

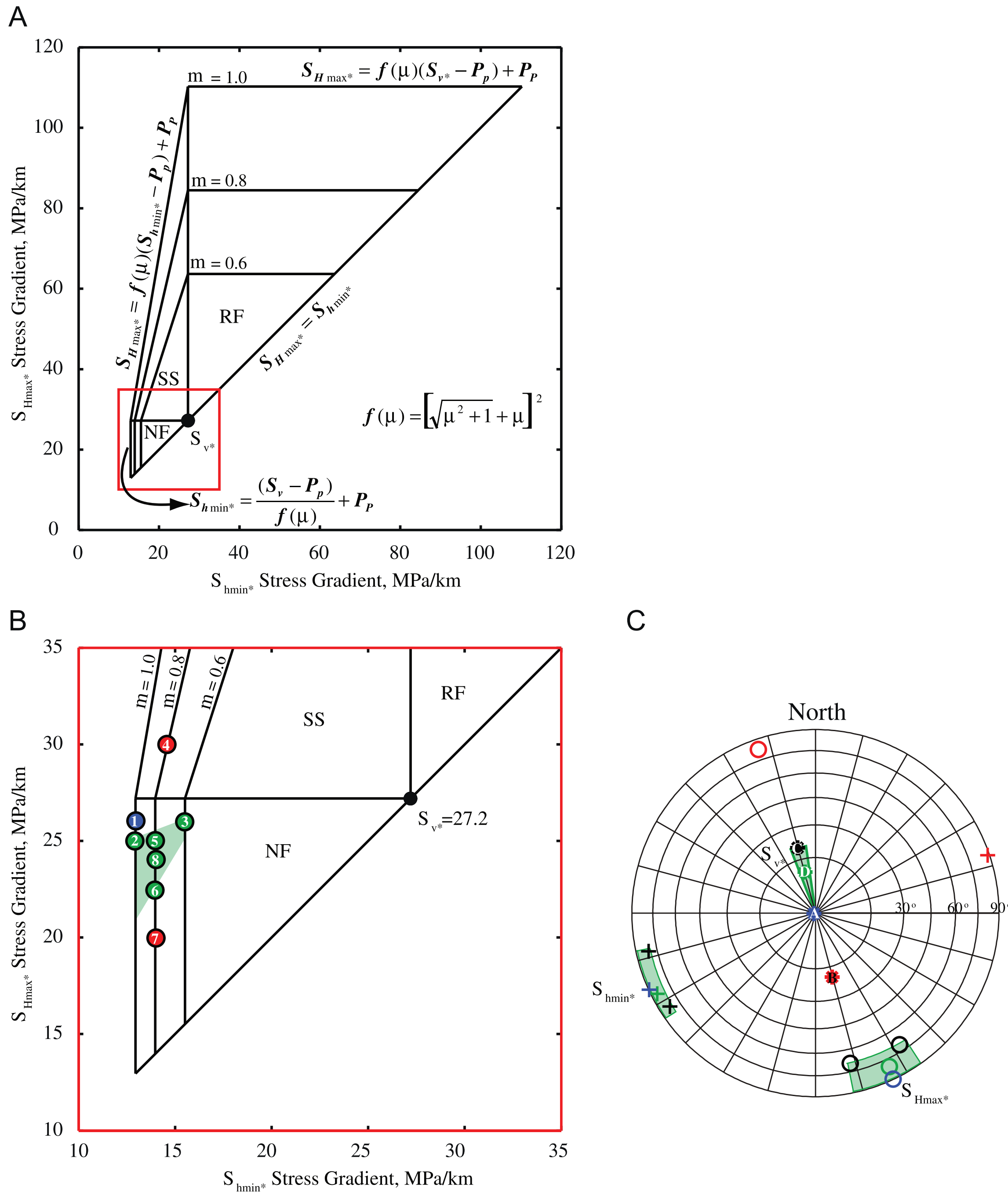

Fig. A1. Constraining the far-field stress state. (A) The "constrain stress" polygons defined by frictional faulting theory for $\mu = 0.6$, 0.8, and 1. The stress regimes are labelled as NF = normal faulting, SS = strike-slip faulting, and RF = reverse faulting. (B) Enlarged view of red box in (A). Stress magnitude parameters for models 1 through 8 that were tested are shown by circles and the acceptable range of stress magnitudes for the far-field stress model is shown by the green-shaded area. The blue circle is the initial stress model, the green circles fall within the acceptable magnitude range for the far-field stress model, and the red circles fall outside the acceptable range of stress magnitudes. (C) Lower hemisphere plot of stress orientations. The green-shaded areas are the acceptable range in orientations for the principal stresses. The blue model (A) is the initial stress model, the red model (B) is not acceptable, the black models (C) were used to test the range in horizontal stress orientations, and the green model (D) is a model with an average acceptable orientation.

We also tested the sensitivity of the modelling to the azimuth of S_1 by rotating the azimuth by $\pm 5°$ from 345°. This slight rotation did not have a significant effect on the modelled failures. However, when S_1 is deviated 20° from vertical towards an azimuth of 165° and S_2 is deviated 20° from horizontal with an azimuth of 335° (stress model 2B in Fig. A1), the breakouts modelled in the LIC118 borehole were positioned at 85° and 265° from the bottom of the hole. The conclusion from these tests was that S_1 is likely deviated up to 10–20° from vertical towards the NNW (Fig. A1c). Because S_1 is nearly vertical, we refer to it as S_{v*}.

The initial stress model also assumed that the stress regime was normal faulting, as indicated in McGarr and Gay [10]. This assumption was tested using model 4D, a strike-slip faulting stress model in which $S_{Hmax*} = 30$ MPa/km $> S_{v*} = 27.2$ MPa/km $> S_{hmin*} = 14$ MPa/km (Fig. A1). Because breakouts form normal to the direction of maximum compression along the borehole, a subhorizontal S_1 acting on a subhorizontal borehole

Table A1
Observed and modelled positions of DITFs and breakouts (BO) in degrees from north for 3 vertical boreholes

Borehole	Image log observations		S_{Hmax^*} Azimuth: 168		S_{Hmax^*} Azimuth: 155		S_{Hmax^*} Azimuth: 148	
	DITF	BO	DITF	BO	DITF	BO	DITF	BO
Site 7V	170		162		156		150	
Site 10		60		80		72		66
Site 13	152	62	167	77	160	70	154	66

results in breakouts modelled closer to the top and bottom of the borehole rather than near the sides of the borehole, as observed. The larger magnitude of S_1 also modelled larger breakout widths (up to 180°) than the observed widths of about 60°. These results are inconsistent with the breakout observations.

A.2. Horizontal stress orientations

In the initial model, the azimuth of S_{Hmax} (S_2) was 155° and S_{hmin} (S_3) was 245°. Since the trajectory of S_{v^*} is likely slightly deviated from vertical, S_2 is also likely to be inclined horizontal, and is, therefore, referred to as S_{Hmax^*}. We tested the effects of rotating the azimuth of S_{Hmax^*} clockwise to 168° and counter-clockwise to 148° (shown by the black open circles in model 2C in Fig. A1) on the borehole failure modelling. Rotating the horizontal stress azimuths had very little effect on the breakouts modelled along the LIC118 borehole. However, it had a significant effect on the orientations of the failures modelled in the near-field vertical boreholes (Table A1). The S_{Hmax^*} azimuth of 148° resulted in a better fit to the observed borehole failure positions at sites 10 and 13, while an azimuth of 168° was more consistent with site 7 V failures. Therefore, the range of acceptable S_{Hmax^*} azimuths was constrained to be between 145° and 168° with an inclination up to 20° from horizontal (Figs. 7 and A1c).

A.3. Vertical stress magnitude

The S_{v^*} magnitude was well constrained based on the density of the overburden material which is about 2700 kg/m^3. Furthermore, the breakouts in the far-field of the LIC118 borehole are primarily controlled by the magnitude S_{v^*} and the uniaxial compressive strength of the rock. In this work, we used a uniaxial compressive rock strength of 200 MPa from laboratory measurements [15] to model the breakouts. Increasing the magnitude of S_{v^*} resulted in breakout widths that were too large and decreasing it resulted in breakout widths that were too small. Based on this analysis, the S_{v^*} gradient ranges from 26.7 to 27.3 MPa/km.

A.4. Pore pressure

The initial stress model had a hydrostatic P_p gradient of 10 MPa/km. This assumption was consistent with the observations that the crust around TauTona is critically stressed. As mentioned above, hydrostatic P_p is typically observed in deep boreholes in low porosity ($<2\%$) and very-low permeability crystalline basement rocks in intraplate regions [22–24]. Without any direct measurements of P_p, we continued to assume P_p is hydrostatic for all the analyses, and to constrain S_3, as discussed in the next section.

A.5. S_{hmin} magnitude

In the initial stress model, the S_3 magnitude was limited by a coefficient of sliding friction of $\mu = 1.0$ in a critically stressed crust. This value of μ is the upper limit of the generally assumed range of μ (0.6–1.0) for the brittle crust [22,27]. Rock mechanics experiments measured a $\mu = 0.82$ for the quartzite and a $\mu = 0.58$ for the cataclasite that is found in the fault trace of many pre-existing faults [14]. The "constrain stress" polygon, which is defined by frictional faulting theory, decreases in size with decreasing values of μ [31] (Fig. A1a). For $P_p = 10$ MPa/km, $S_{v^*} = 27.2$ MPa/km, and $\mu = 1$, the lower limit of S_{hmin^*} is 12.9 MPa/km, while if $\mu = 0.6$, S_{hmin^*} is limited to 15.5 MPa/km.

To test the magnitude of S_{hmin^*}, we analysed the borehole failure modelling results based on BEM calculations using stress models 2D and 3D (Fig. A1). For the LIC118 borehole, both stress models predicted breakouts consistent with the far-field observations. Model 2D ($\mu = 1.0$) is more consistent with the near-field observations. The breakout widths predicted at sites 10 and 13 and at the top of LIC118 more closely matched the observations. The DITFs at site 10 and 7 V were also better represented with stress model 2D. There was no significant difference between the two models in the other boreholes. While model 3D was less consistent with the near-field observations, it could not be ruled out. For this reason, the S_{hmin^*} gradient was constrained to be between 12.9 and 15.5 MPa/km (Figs. 8 and A1b).

A.6. S_{Hmax} magnitude

The initial stress model assumed that *the* $S_{Hmax} \gg S_{hmin}$. To test this assumption, we compared the failure predictions from three stress models: 5D, 6D, and 7D, where the S_{Hmax^*} gradients are 25, 22.5, and 20 MPa/km, respectively (Fig. A1). All the stress models predicted borehole failures that were consistent with the far-field breakout observations in the LIC118 borehole. In general, the borehole failure models based on the BEM calculations using the smaller S_{Hmax^*} gradients better represented the absence of breakouts that was observed at the top of the LIC118 (Fig. 6), but were not as consistent with the other near-field observations. The borehole failure modelling based on stress model 7D predicted the absence of failures at the top of the LIC118 borehole and the breakouts at site 10, but does not predict any breakouts at site 13 or any DITFs at site 7 V. Because of the lack of consistency with the near-field borehole observations, we excluded stress model 7D from the range of acceptable far-field stress states. We constrained the range of S_{Hmax^*} gradients for a gradient of S_{hmin^*} of 14 MPa/km ($\mu = 0.8$) to be 22.5–25.5 MPa/km. The acceptable S_{Hmax^*} range is smaller (25–26 MPa/km) for an S_{hmin^*} of 15.5 MPa/km ($\mu = 0.6$) and larger (21–25) for an S_{hmin^*} of 13 ($\mu = 1.0$) (as shown in the green shaded regions of Figs. 8 and A1b).

References

[1] Gane PG, Hales AL, Oliver HA. A seismic investigation of the Witwatersrand earth tremors. Bull Seismol Soc Am 1946;36:49–80.
[2] Gane PG, Seligman P, Stephen JH. Focal depths of Witwatersrand tremors. Bull Seismol Soc Am 1952;42:239–50.
[3] McGarr A, Spottiswoode SM, Gay NC. Relationship of mine tremors to induced stresses and to rock properties in the focal region. Bull Seismol Soc Am 1975;65:981–93.
[4] Reches Z. Building a natural earthquake laboratory at focal depth. In: Proceedings IODP-ICDP Fault Zone Drilling Workshop. Miyazaki, Japan, 2006.

[5] Reches Z, Ito H. Scientific drilling of active faults: past and future. Berlin: Springer; 2007.
[6] Reches Z, Jordan TH, Johnston MJ, Zoback M. Drilling across active faults in deep mines in South Africa for monitoring earthquake processes in the near-field. Eos Trans. AGU Fall Mtg Suppl 2005;86 [Abstract T43D-01].
[7] Gay NC. Principal horizontal stresses in southern Africa. Pure Appl Geophys 1977;115:3–10.
[8] Gay NC. Virgin rock stresses at Doornfontein gold mine, Carletonville, South Africa. J Geol 1972;80:61–80.
[9] Gay NC. In-situ stress measurements in southern Africa. Tectonophysics 1975;29:447–59.
[10] McGarr A, Gay NC. State of stress in the earth's crust. Ann Rev Earth Planet Sci 1978;4:405–36.
[11] Peska P, Zoback MD. Compressive and tensile failure of inclined wellbores and determination of in-situ stress and rock strength. J Geophys Res-Solid Earth 1995;100:12791–811.
[12] Zoback MD, Barton CB, Brudy M, Castillo D, Finkbeiner T, Grollimund BR, et al. Determination of stress orientation and magnitude in deep wells. Int J Rock Mech Min Sci 2003;40:1049–76.
[13] Stacey TR, Wesseloo J. Applications of indirect stress measurement techniques (non strain gauge based technology) to quantify stress environments in mines. Safety in mines research advisory committee. Univ Witwatersrand SRK Consult 2002;GAP858:1–67.
[14] Cartwright P, Walker G. In-situ stress measurement, 83 level shaft pillar area, TauTona mine, AngloGold. 2000.
[15] Heesakkers V, Lockner D, Reches Z. The rupture of an m2.2 earthquake within the mechanically heterogeneous Pretorius fault-zone, Tautona mine, South Africa (NELSAM project). In: Proc Eur Geosci. Vienna: Union General Assembly; 2007.
[16] Hofmann GF, Murphy SK. Coulomb stress triggering in the underground mining environment. Vancouver; 2007.
[17] Wiles TD. Map3D user's manual. Mine modelling (Pty) 2005.
[18] Wiles TD, Lachenicht R, van Aswegen G. Integration of deterministic modelling with seismic monitoring for the assessment of rock mass response to mining: Part I theory. Johannesburg 2000.
[19] Wiles TD. Rockburst prediction using numerical modelling-realistic limits for failure prediction accuracy. Australia: 2005.
[20] Wiles TD. Reliability of numerical modelling predictions. Int J Rock Mech Min Sci 2006;43:454–72.
[21] Zoback ML, Zoback MD, Adams J, Assumpcao M, Bell S, Bergman EA, et al. Global patterns of tectonic stress. Nature 1989;341:291–8.
[22] Townend J, Zoback MD. How faulting keeps the crust strong. Geology 2000; 28:399–402.
[23] Coyle BJ, Zoback MD. In situ permeability and fluid pressure measurements at approximately 2-km depth in the Cajon pass research well. Geophys Res Lett 1988;15:1029–32.
[24] Huenges E, Erzinger J, Kuck J. The permeable crust: geohydraulic properties down to 9101 m depth. J Geophys Res 1997;102:18255–65.
[25] Barton CA, Zoback MD. Stress perturbations associated with active faults penetrated by boreholes—possible evidence for near-complete stress drop and a new technique for stress magnitude measurement. J Geophys Res-Solid Earth 1994;99:9373–90.
[26] Shamir G, Zoback MD. Stress orientation profile to 3.5 km depth near the San-Andreas fault at Cajon Pass, California. J Geophys Res-Solid Earth 1992;97: 5059–80.
[27] Byerlee JD. Friction of rock. Pure Appl Geophys 1978;116:615–26.
[28] Reches Z, Baer G, Hatzor Y. Constraints on the strength of the upper crust from stress inversion of fault slip measurements. J Geophys Res 1992;97: 481–93.
[29] Zoback MD, Townend J, Grollimund BR. Steady-state failure equilibrium and deformation of intraplate lithosphere. Int Geol Rev 2002;44:383–401.
[30] Keilis-Borok VI. On estimation of the displacement in an earthquake source and of source dimension. Ann Geofis 1959;12:205–14.
[31] Moos D, Zoback MD. Utilization of observations of wellbore failure to constrain the orientation and magnitude of crustal stresses-application to Continental, Deep-Sea Drilling Project, and Ocean Drilling Program boreholes. J Geophys Res-Solid Earth Planets 1990;95:9305–25.